Size dependence of the carrier ground state of small semiconductor particles

Size dependence of the carrier ground state of small semiconductor particles

Takeshi Inaoka

Department of Materials Science and Technology, Faculty of Engineering, Iwate University, 4-3-5 Ueda, Morioka, Iwate 020, Japan

Abstract. By calculating the carrier density distribution and the effective one-particle potential self-consistently, we investigate the size dependence of the carrier ground state of small spherical semiconductor particles with the doping level fixed. The particles are assumed to be in an insulating medium or in the vacuum. The prominent peak just inside the carrier-deficient surface layer in the carrier density profile persists regardless of the particle size, while, with increasing size, the oscillatory density-profile feature inside the prominent peak becomes less and less conspicuous and reduces to nearly constant density to achieve charge neutrality. The remarkable variation of the potential bending with increase of the size depends upon where the newly occupied carrier states have their probability density concentrated. This variation of the potential bending often involves the energy intersection of two close energy levels with different angular momenta l.

1. Introduction

Small particles of metals and semiconductors exhibit interesting physical properties inherent in small systems, such as the surface effect and the quantum size effect. Examining the size dependence of electronic properties of small particles is helpful to understand how electronic properties evolve from atomic-like to bulk-like features with increasing size. As for small metal particles, ground-state properties [1–4] and static [3, 5, 6] or dynamic [3, 6–9] response properties of confined conduction electrons were theoretically investigated on the basis of the spherical jellium-background model (SJBM) combined with the density-functional theory [1–5, 7, 9], the random-phase approximation (RPA) [6] or the RPA sum-rule approach [8]. The SJBM gives a good description of metal clusters with high lattice symmetry, and allows us to perform the self-consistent calculation up to large sizes which go beyond the applicability of more sophisticated first-principles calculations. In relation to ground-state properties, the above theoretical analysis clearly shows the stability of metal clusters at shell-closing electron numbers [4] and the electronic shell effect on the size dependence of the ionization potential [1, 2, 4]. These results support the experimental observations [10, 11]. On the other hand, it seems that theoretical studies of carrier states of semiconductor particles have not been so advanced as those of electronic states of metal particles, although there is a hydrodynamic approach to coupling of surface carrier plasmons with surface polar phonons in spherical semiconductor particles [12]. On the experimental side, coupled modes of carrier plasmons and polar phonons in semiconductor particles were observed by Raman scattering [13] and infrared absorption [13, 14].

Our letter [15] has already highlighted characteristics of the carrier ground state of small semiconductor particles and emphasized the difference from the conduction-electron ground

state of metal particles. We consider the carrier ground state of small doped-semiconductor particles that lie in an insulating medium or in the vacuum. The first characteristic point is the boundary condition for carriers at the surface of the semiconductor particle. The kinetic energy of each carrier (tens of meV or less) is much smaller than the barrier potential at the interface with the insulating medium or the work function (several eV). Therefore, the characteristic length of the carrier density profile near the surface (tens of Å or longer) is much longer than the penetration length of carriers into the surrounding medium or the vacuum (one or a few Å). The second point is the effect of the dielectric polarization of the particle background which accommodates carriers. The polarization of this dielectric background reduces the Coulomb interaction between carriers. In addition, when a carrier approaches the particle surface, it is affected by the image potential that arises from the difference between the dielectric constant of the particle background and that of the surrounding medium or the vacuum.

The aim of the present work is to investigate the size dependence of the carrier ground state of small semiconductor particles with the doping level fixed. We calculate the carrier density distribution and the effective one-particle potential self-consistently by means of the standard density-functional theory involving the local-density approximation (LDA) [16]. As in our letter [15], our objects of calculation are spherical n-type GaAs particles in an insulating medium or in the vacuum. Each particle is composed of the carriers and the spherical background that is dielectric and electrically positive. The dielectric polarization of the background can be described by the static dielectric constant ε_0. The ionized donors are assumed to be smeared out into a homogeneous positive charge distribution, as the positive ions in a metal cluster are treated in the same fashion in the SJBM. Taking account of the above-mentioned boundary condition for carriers, we assume that the carriers are confined in the particle by an infinite barrier potential at the surface of the particle, namely, that envelope wave functions of carriers vanish at the surface. The same assumption for the boundary condition was made in order to explore carrier states at the flat semiconductor surface [17] or at the flat oxide–semiconductor interface [18]. In n-doped compound semiconductors, such as n-GaAs, n-InSb and n-InAs, carriers easily become degenerate with increase of the doping level, because an extremely small effective mass and a large dielectric constant give a large effective Bohr radius a_B^*, which leads to a small effective carrier density parameter r_s. Our calculations deal with such highly degenerate carriers.

The image potential depends upon the static dielectric constant ε_m which characterizes the surrounding medium. We evaluate the effect of the image potential by comparing the result for $\varepsilon_m = 1$ with that for $\varepsilon_m = \varepsilon_0$ (no image potential).

To estimate the geometric effect due to curvature of the sphere, we also calculate the carrier ground state of an n-doped GaAs film with the same doping level by virtue of the same calculational scheme which involves the effect of the image potential.

The greater part of the present work is devoted to electrically neutral particles where the number of carriers is balanced with that of ionized donors. However, the particle may exchange carriers with its surroundings and may be ionized as a whole. To gain some insight into this situation, we compare the carrier state of a neutral particle with that of a donor-superfluous or donor-deficient particle with the same number of carriers in the same configuration.

2. Theory

In this section, we represent the theoretical framework for the present analysis. A brief explanation has already been given in our letter [15]. As is stated in the previous section,

we consider spherical doped-semiconductor particles in an insulating medium or in the vacuum that have highly degenerate carriers restrained in the particle by an infinite barrier potential at the particle surface.

We employ the standard density-functional formalism which involves the LDA. The ground state of carriers can be obtained by solving the following equations self-consistently:

$$\{-(\hbar^2/2m^*)\Delta + V_{\text{eff}}[r; n(r)]\}\psi_i(r) = E_i\psi_i(r) \tag{1}$$

$$n(r) = \sum_{i=1}^{N} |\psi_i(r)|^2 \tag{2}$$

where m^*, N, $n(r)$, $\psi_i(r)$, and E_i denote the effective mass of carrier electrons, the number of carriers, the carrier number density at position r, and the Kohn–Sham [16] single-particle eigenfunctions and eigenenergies, respectively. The effective one-particle potential V_{eff} consists of the electrostatic Hartree potential V_{H}, the image potential V_{im}, and the exchange–correlation potential V_{xc}. These potential components are expressed as

$$V_{\text{H}}[r; n(r)] = \frac{e^2}{\varepsilon_0} \int \mathrm{d}^3r' \frac{n(r') - n^+}{|r - r'|} \tag{3}$$

$$V_{\text{im}}(r) = \frac{\varepsilon_0 - \varepsilon_{\text{m}}}{2\varepsilon_0} \frac{e^2}{R} \sum_{k=1}^{\infty} \frac{k+1}{k(\varepsilon_0 + \varepsilon_{\text{m}}) + \varepsilon_{\text{m}}} \left(\frac{r}{R}\right)^{2k} \tag{4}$$

and

$$V_{\text{xc}}[n(r)] = -(e^2/2\varepsilon_0 a_{\text{B}}^*)(2/\pi)(\tfrac{9}{4}\pi)^{1/3}\{1/r_{\text{s}}(r) + 0.0545\ln[1 + 11.4/r_{\text{s}}(r)]\}. \tag{5}$$

In equations (3)–(5), R, ε_0, ε_{m}, and n^+ signify the radius of the spherical particle, the static dielectric constant of the particle background, the static dielectric constant of the surrounding medium, and the uniformly spread-out density of ionized donors, respectively. We adopt the spherical polar coordinates and locate the origin at the centre of the particle. The effective Bohr radius a_{B}^* and the local effective density parameter $r_{\text{s}}(r)$ are defined by

$$a_{\text{B}}^* = \varepsilon_0 \hbar^2 / m^* e^2$$

and

$$a_{\text{B}}^* r_{\text{s}}(r) = [3/4\pi n(r)]^{1/3}$$

respectively. For the exchange–correlation potential, we invoke the expression parametrized by Gunnarsson and Lundqvist [19].

Equation (4) can be converted into the form

$$V_{\text{im}}(r) = \frac{1}{2\varepsilon_0} \frac{\varepsilon_0 - \varepsilon_{\text{m}}}{\varepsilon_0 + \varepsilon_{\text{m}}} \frac{e^2}{R} \left(\frac{(r/R)^2}{1 - (r/R)^2} - \frac{\varepsilon_0}{\varepsilon_0 + \varepsilon_{\text{m}}} \ln[1 - (r/R)^2] \right.$$

$$\left. - \frac{\varepsilon_0 \varepsilon_{\text{m}}}{\varepsilon_0 + \varepsilon_{\text{m}}} \sum_{k=1}^{\infty} \frac{(r/R)^{2k}}{k[k(\varepsilon_0 + \varepsilon_{\text{m}}) + \varepsilon_{\text{m}}]} \right). \tag{6}$$

It is an excellent approximation to take only the first few terms in the summation of equation (6). We retain the first two terms ($k = 1$ and 2) and neglect higher-order terms in the following calculations.

Our calculations are concerned with the spherically symmetric system.   When the effective potential V_{eff} is spherically symmetric, the angular part of each energy eigenfunction is described by a spherical harmonic $Y_{lm}(\theta, \varphi)$, and the radial part can be obtained from the differential equation

$$\{-[(\hbar^2/2m^*)/r^2](d/dr)(r^2 d/dr) + l(l+1)\hbar^2/2m^*r^2 + V_{eff}[r; n(r)]\}\tilde{R}_l(r) = E_l \tilde{R}_l(r). \quad (7)$$

There is a series of energy levels for each value of l ($l = 0, 1, 2, \ldots$), which we label as $n = 1, 2, 3, \ldots$ in order of increasing energy. Each energy eigenstate is specified by n, l, and m, namely, the radial, the orbital-angular-momentum, and the magnetic quantum numbers. Because of the spherical symmetry, energy eigenstates are degenerate with respect to m, and each energy eigenvalue is assigned only by n and l. If the $2(2l+1)$-fold degenerate states including spin for each occupied energy level are all occupied (closed-shell configuration), we have the spherical carrier density distribution, which leads to the spherical potential V_{eff}. The carrier density $n(r)$ can be constructed by

$$n(r) = 2 \sum_{n,l,m}' |\psi_{nlm}(r)|^2 = \frac{1}{2\pi} \sum_{n,l}' (2l+1)|\tilde{R}_{nl}(r)|^2 \qquad (8)$$

where $\tilde{R}_{nl}(r)$ denotes the radial part of the eigenfunction $\psi_{nlm}(r)$, and the primed summation is performed over the occupied energy eigenstates (n, l, m) or levels (n, l). If the degenerate states for the highest occupied level are not all filled (open-shell configuration), the carrier density distribution given by equation (2) and the resulting potential V_{eff} are not spherically symmetric. To retain the spherical symmetry, however, we employ the manipulation of replacing $|\psi_{nlm}(r)|^2$ in equation (8) by its average over m, that is,

$$\frac{1}{2l+1} \sum_{m=-l}^{l} |\psi_{nlm}(r)|^2 = \frac{1}{4\pi}|\tilde{R}_{nl}(r)|^2. \qquad (9)$$

This manipulation creates the spherical carrier density distribution by averaging over all the multiplets, and it enables the self-consistent calculation within the spherical symmetry for open-shell configurations also. This averaging scheme to preserve the spherical symmetry was used in the LDA calculation of electronic states of small metal particles on the basis of the SJBM [1–4].

To solve equation (7), it is convenient to expand $\tilde{R}_l(r)$ in a series of normalized spherical Bessel functions $\tilde{j}_l$:

$$\tilde{R}_l(r) = \sum_{k=1}^{\infty} A_k \tilde{j}_l\left(\alpha_{lk}\frac{r}{R}\right) \qquad (10)$$

where $\tilde{j}_l(\alpha_{lk}r/R)$ is expressed as

$$\tilde{j}_l(\alpha_{lk}r/R) = \sqrt{2/R^3}\, j_l(\alpha_{lk}r/R)/j_{l+1}(\alpha_{lk}) \qquad (11)$$

in terms of spherical Bessel functions $j_l(x)$, α_{lk} ($k = 1, 2, 3, \ldots$) is the kth zero of $j_l(x)$, and $\tilde{j}_l$ is normalized as

$$\int_0^R dr\, r^2 \tilde{j}_l\left(\alpha_{lk}\frac{r}{R}\right) \tilde{j}_l\left(\alpha_{lk'}\frac{r}{R}\right) = \delta_{kk'}. \qquad (12)$$

Equation (10) satisfies the boundary condition that $\tilde{R}_l(r)$ should vanish at $r = R$. With the expansion (10), equation (7) is transformed into the matrix eigenvalue problem

$$\sum_{k'=1}^{\infty} \left[\frac{\hbar^2}{2m^*} \left(\frac{\alpha_{lk}}{R} \right)^2 \delta_{kk'} + P_{kk'} \right] A_{k'} = E_l A_k \tag{13}$$

where $P_{kk'}$ is defined by

$$P_{kk'} = \int_0^R dr \, r^2 \tilde{j}_l \left(\alpha_{lk} \frac{r}{R} \right) V_{\text{eff}}[r; n(r)] \tilde{j}_l \left(\alpha_{lk'} \frac{r}{R} \right). \tag{14}$$

For numerical calculations, we truncate the infinite series (10) and retain a finite number of terms up to an appropriate order. We take 30–50 terms in the following calculations. To gain the self-consistent solution, we employ the standard iteration scheme that starts with a trial potential of V_{eff} and is repeated until self-consistency is achieved.

3. Results and discussion

We explore the size dependence of the carrier ground state by varying the radius of the particle and the number of carriers with the doping level fixed. Figure 1 exhibits the carrier density profile $n(r)$ and the effective potential $V_{\text{eff}}(r)$ for various sizes of electrically neutral n-type GaAs particles with closed-shell configurations. The fixed doping level corresponds to the bulk carrier concentration $n_b = 5 \times 10^{17}$ cm^{-3}, that is, to the effective carrier density parameter $r_s = 0.7671$. The parameter values used in our calculations are the effective electron mass ratio $m^*/m_e = 0.067$ and the static dielectric constant $\varepsilon_0 = 12.9$. The static dielectric constant of the surrounding medium is taken to be $\varepsilon_m = 1$ except for some cases where the image potential is switched off by setting $\varepsilon_m = \varepsilon_0$.

The carrier density distribution for each size is shown by the full curve in the upper panels of figure 1. The horizontal broken line in each upper panel denotes the density of the homogeneously spread-out ionized donors. The length is scaled by the effective Bohr radius $a_B^* = \varepsilon_0 \hbar^2 / m^* e^2 = 101.9$ Å. In figure 1(a) and (b), the dotted curves labelled with (n, l) represent the decomposition of $n(r)$ into components of various (n, l) shells. In figure 1(c)–(j), the dotted curves with only l assigned display the resolution of $n(r)$ into l components, and some of these curves result from more than one shell. The dotted curves labelled 'SW' in figure 1(b), (f), and (h) show the density distribution of the carriers confined in a square-well potential $V(r) = 0$ for $r < R$ and $V(r) = \infty$ for $r > R$. The dotted curves labelled 'no V_{im}' in figure 1(a), (d), and (g) exhibit the carrier density distribution obtained from the self-consistent calculation in the absence of the image potential. The dotted curve labelled 'no V_{xc}' in figure 1(e) represents the carrier density distribution obtained from the self-consistent calculation taking no account of the exchange–correlation potential. The dotted curve labelled 'film' in the upper panel of figure 1(j) indicates the carrier density distribution in the film whose thickness is equal to the diameter of the particle. Here the z axis is taken to be normal to the surface, and its origin is located right in the middle of the film. Aside from the geometric difference, we employ the same calculational scheme in this film calculation as in the present calculation for small particles [20]. This film calculation includes the effect of the image potential.

The effective potential and the occupied energy levels for each size are displayed by the full curve and the horizontal full bars, respectively, in each lower panel of figure 1(a)–(j). The energy of V_{eff} is measured from its value at $r = 0$ and scaled in units of
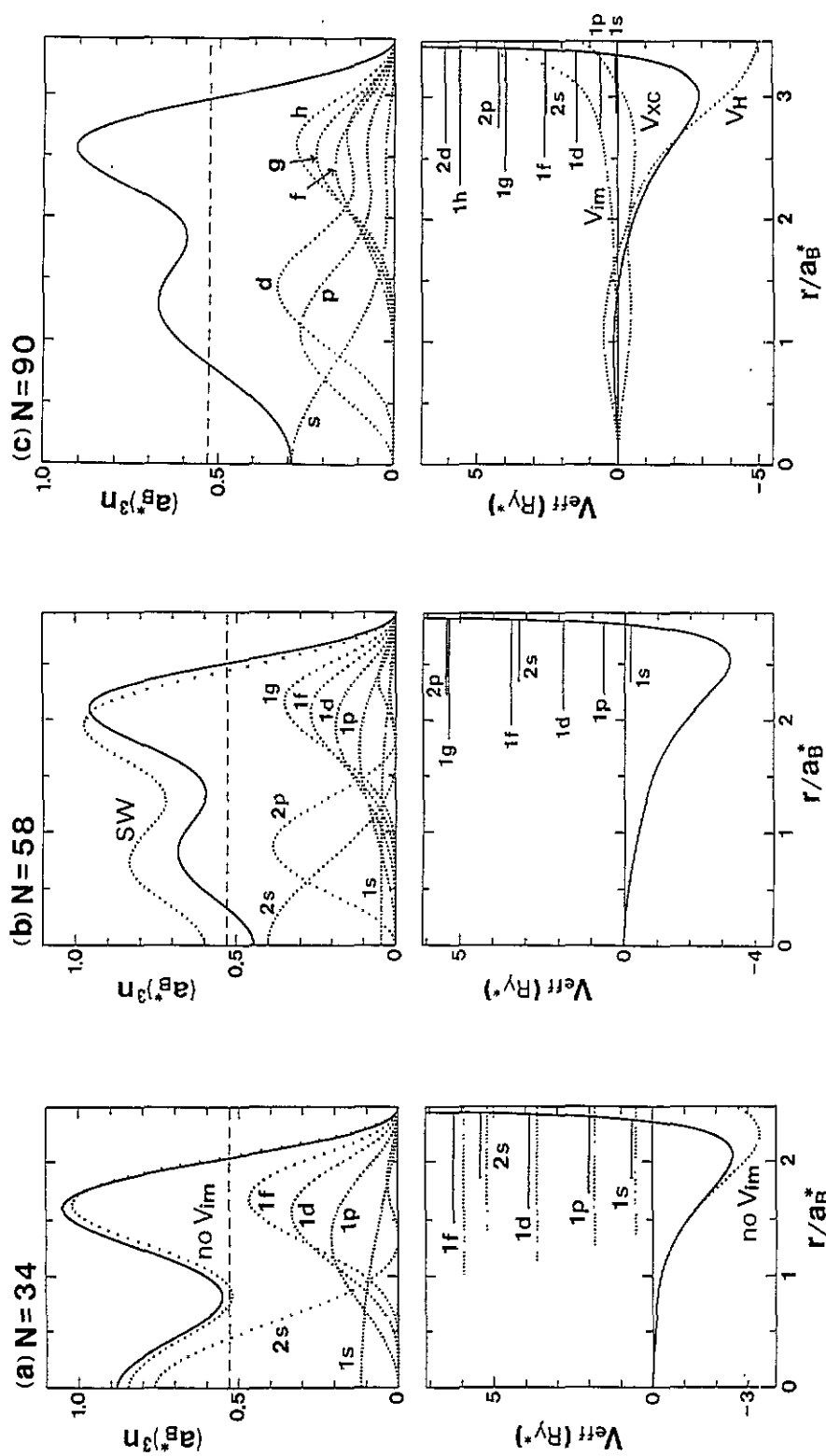
Figure 1. The size dependence of the carrier ground state of spherical n-type GaAs particles with closed-shell configurations. For details, see the text.
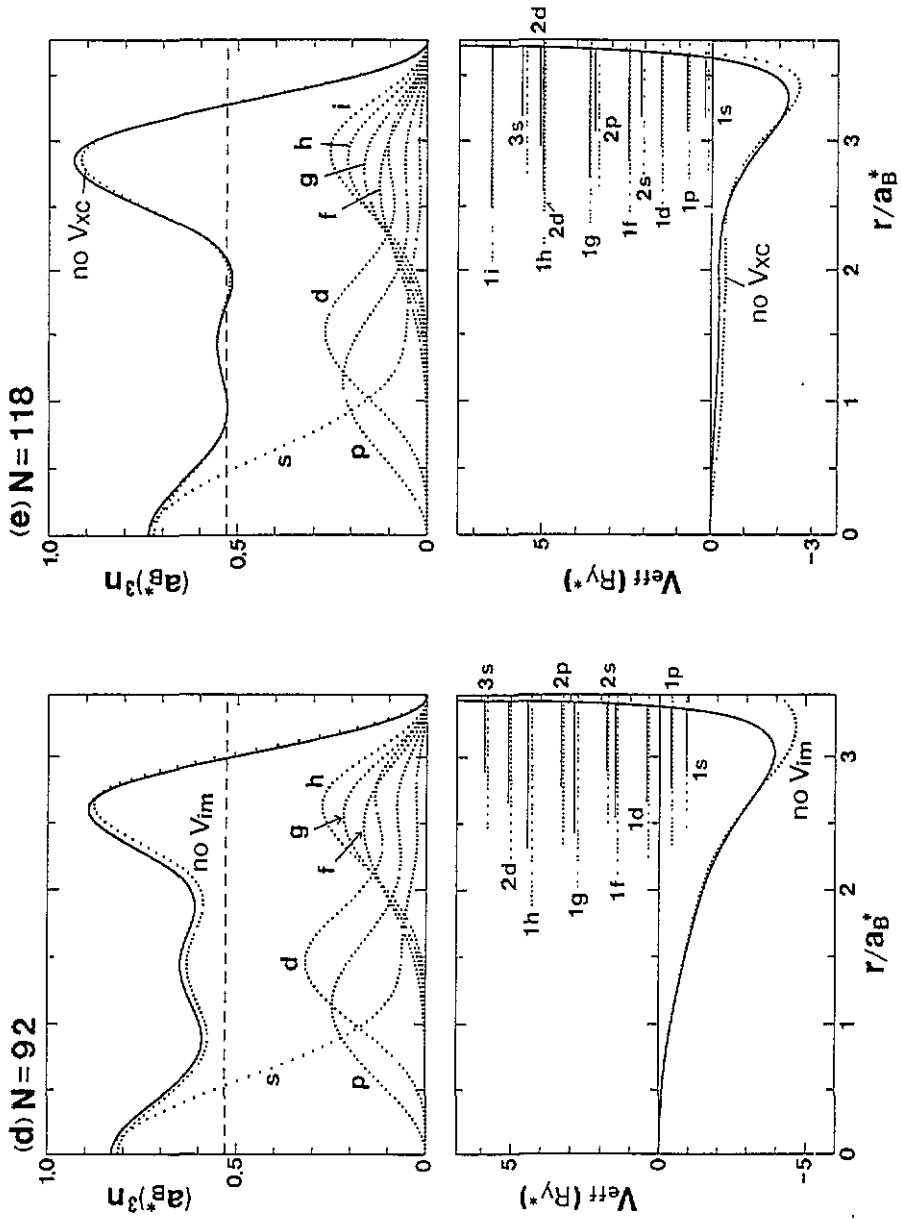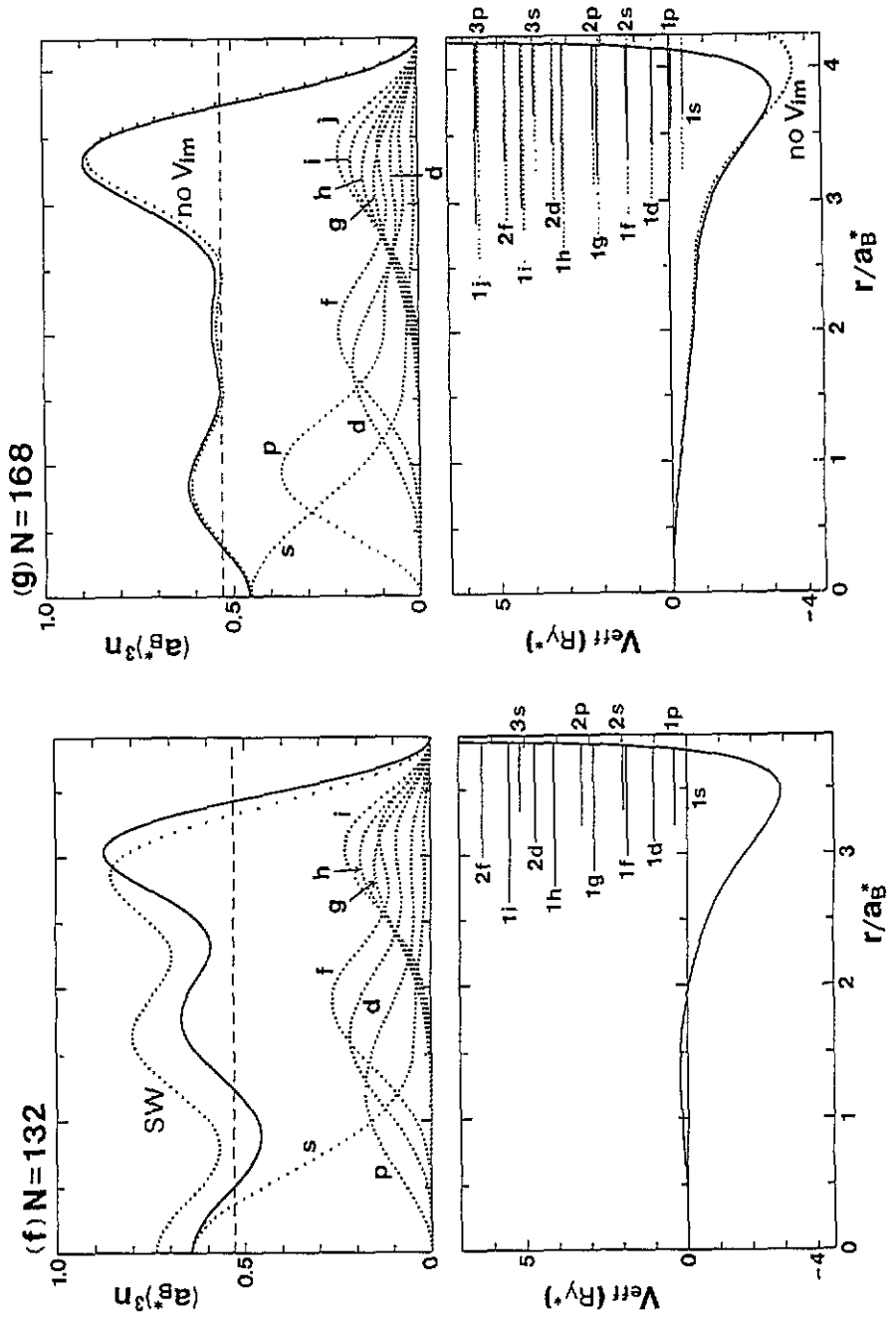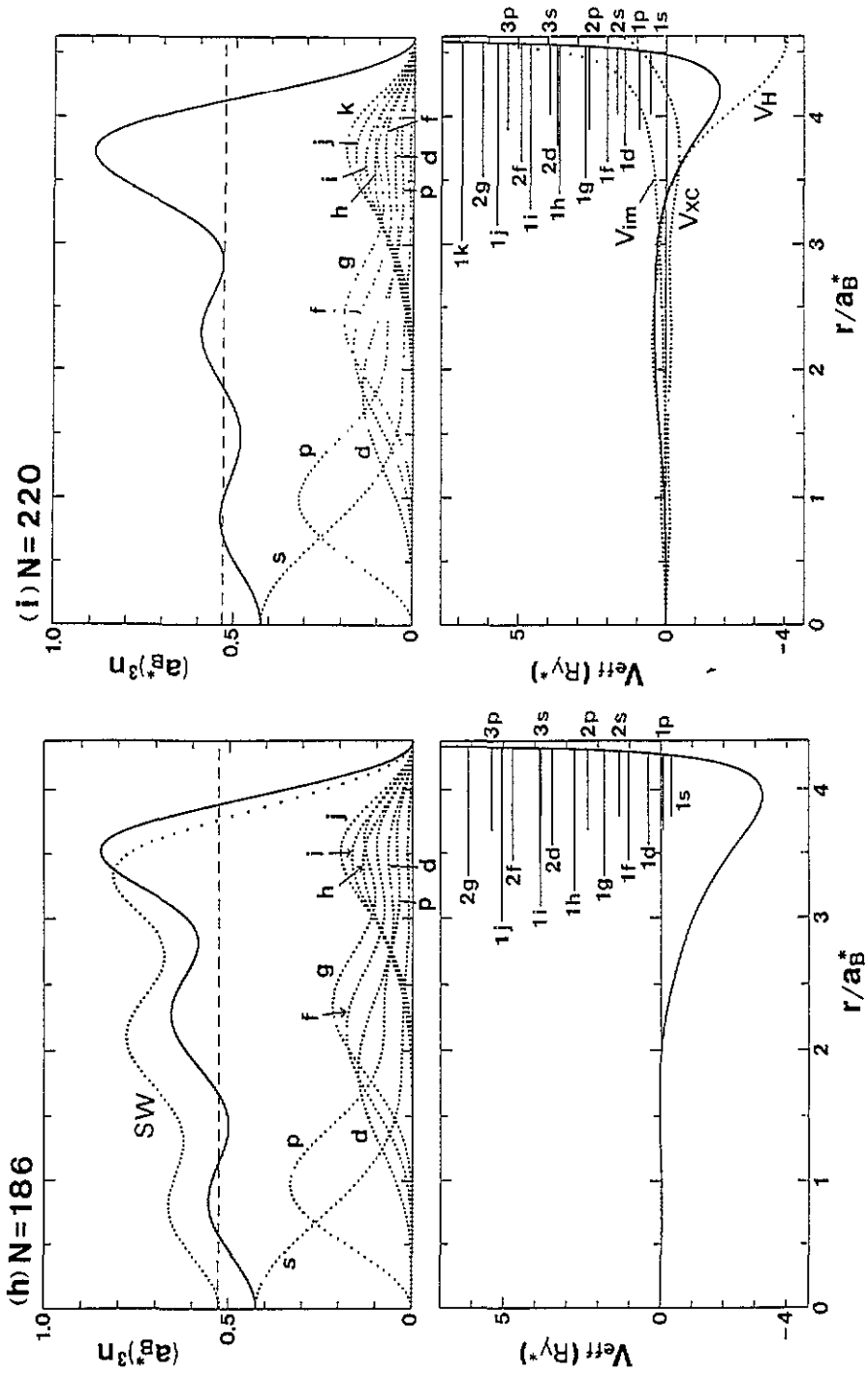
Figure 1. (Continued)

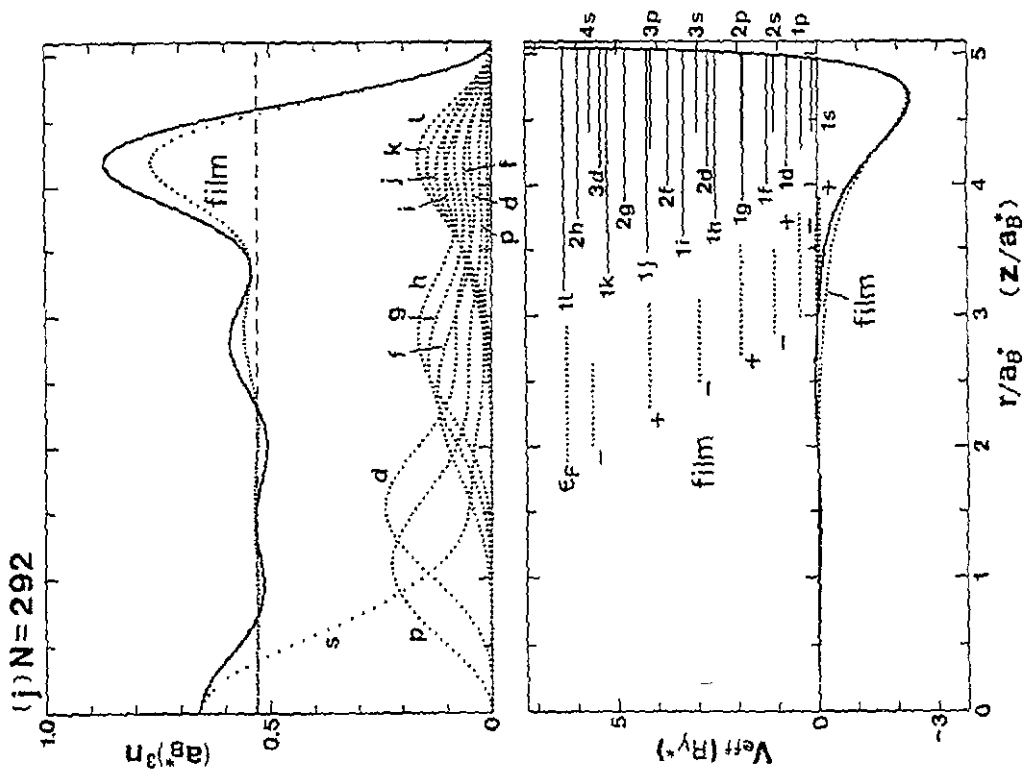Figure 1. (Continued)

Figure 1. (Continued)

Figure 1. (Continued)

$Ry^* = e^2/2\varepsilon_0 a_B^* = 5.478$ meV. An energy level of higher l is displayed as a longer bar. Each energy level of l consists of $2(2l + 1)$-fold degenerate states, which are all occupied because each carrier system in this figure has a closed-shell configuration. In figure 1(*a*), (*d*) and (*g*), the dotted curves and bars represent the effective potential and the occupied energy levels in the absence of the image potential. In figure 1(*c*) and (*i*), the effective potential is decomposed into three components V_H, V_{xc} and V_{im}. In figure 1(*e*), the dotted curve and bars show the effective potential and the occupied energy levels in the absence of the exchange–correlation potential. The 2d and 1h energy levels almost overlap each other. In figure 1(*j*), the dotted curve and bars exhibit the effective potential, the subband bottoms, and the Fermi energy for the film. Because of the reflection symmetry, the surface-normal part of the eigenfunction for each subband becomes even or odd with respect to the reflection operation $z \rightarrow -z$, as specified by the plus or minus sign. Note that the origin of the z axis is placed in the middle of the film.

The quantum numbers n and l are related to the features in the probability density profile of the corresponding shell. As is shown typically in the upper panel of figure 1(*b*), only s shells ($l = 0$) make a finite contribution to the carrier density at the centre, and the number $n - 1$ is equal to the node number of the radial wave function in the range $0 < r < R$. The 1p, 1d, 1f, and 1g components of the carrier density vanish only at the surface and the centre, and have no nodes in the intermediate range $0 < r < R$. The component of higher l among these four is more localized near the surface. The 2s and 2p components have one node in the range $0 < r < R$, which leads to the two-peak structure in the profile. The peak at or near the centre is much larger than the other. Some l-component curves in figure 1(*c*)–(*j*) involve more than one shell. However, in the light of the above-mentioned profile features of (n, l) shells, we can roughly decompose each of these l-component curves into contributions of a few constituent shells.

First, we pay attention to the carrier density distribution (see the full curve in each upper panel of figure 1(*a*)–(*j*)). The value of the carrier density falls and vanishes at the surface, which produces a carrier-deficient surface layer with positive charges. Just inside this surface layer appears a prominent peak whose magnitude is considerably larger than the homogeneous donor density.

As is seen from the dotted curves 'sw' in figure 1(*b*), (*f*), and (*h*), there is a great excess of negative carrier charges inside the carrier-deficient surface layer, when carriers are confined in the square-well potential. Of course, this is not a self-consistent solution. To reach self-consistency, a considerable fraction of internal excess carriers transfer to the surface region, which leads to the prominent peak near the surface. This implies that free carriers tend to achieve charge neutrality inside the prominent peak, and that interior excess carriers, if any, tend to transfer to the surface region to screen the positive charges in the carrier-deficient surface layer.

The Friedel oscillation in the carrier density profile is more conspicuous at smaller sizes. Its form varies significantly as one shell after another is occupied with increasing size. The newly occupied shell creates a corresponding new feature in the profile. Once a shell is completely filled, its component in the profile declines gradually in magnitude, because a fixed number of carriers in the shell extend in the larger region with increasing size. The prominent peak just inside the carrier-deficient surface layer is mainly made up of the shells with $n = 1$ and higher l whose substantial probability density is well localized near the surface. When the carrier number increases from $N = 90$ to 92 with slight increase of the size (see figure 1(*c*) and (*d*)), the 3s shell is newly occupied, which gives rise to a pronounced peak around the centre. The probability density of the 3s shell has an intense peak around the centre, as is shown by figure 3 and its caption in [15]. When

N is raised from 92 to 118 with appreciable increase of the size, the carriers in already closed shells spread over the larger region, which results in the rigid downward shift of the profile curve in the range $r/a_{\mathrm{B}}^* \lesssim 2$. The newly occupied 1i shell, whose probability density is concentrated near the surface, acts to enhance the intensity of the outermost peak in the profile. The variation of the oscillatory pattern with increase of the size can be understood in the same manner in other ranges of the size also. The Friedel oscillation inside the outermost peak becomes less and less conspicuous with increasing size. The converging profile is characterized by the prominent peak just inside the carrier-deficient surface layer and the almost constant density inside the prominent peak to achieve charge neutrality. In figure 1(j), the result of the film calculation is presented in parallel with that of the particle calculation. This indicates that the Friedel oscillation is much less conspicuous in the case of the film. This is consistent with the fact that the Friedel oscillation at the flat surface of the semi-infinite metal is quite modest compared with that in the small metal particle (see figures 3 and 4 in [2]).

Here we mention the effect of the image potential expressed by equation (4). In general the inequality $\varepsilon_0 > \varepsilon_{\mathrm{m}}$ is satisfied because the semiconductor has quite a large dielectric constant ε_0. In this case, the image potential operates to repel the carrier into the inside of the particle, when it approaches the surface. As ε_{m} increases with ε_0 fixed, the image potential acts less effectively, and vanishes when ε_{m} becomes equal to ε_0. We can infer the intermediate case $1 < \varepsilon_{\mathrm{m}} < \varepsilon_0$ from the two typical cases $\varepsilon_{\mathrm{m}} = 1$ and $\varepsilon_{\mathrm{m}} = \varepsilon_0$ (see figure 1(a), (d), and (g)). As the image potential reduces its repulsive effect, a small fraction of interior carrier charges shift to the surface region, because carriers can get closer to the surface.

For a somewhat quantitative analysis, we introduce the radial dipole which is defined by

$$P_{\mathrm{r}} = \frac{a_{\mathrm{B}}^*}{4\pi R^2} \int \mathrm{d}^3 r \, r [n^+ - n(r)]. \tag{15}$$

Figure 2 exhibits the size dependence of the radial dipole obtained from the full self-consistent calculation involving the image potential (filled circles), the self-consistent calculation in the absence of the image potential (open triangles), and the non-self-consistent calculation assuming the square-well potential (open squares). Larger filled circles, all open triangles, and larger open squares correspond to closed-shell configurations, while smaller filled circles and smaller open squares correspond to open-shell configurations. One or some serial open-shell points between two neighbouring closed-shell points are nearly on the line connecting the two closed-shell points. The newly occupied shell is specified at each closed-shell point. The two or three shells are indicated at $N = 58$, 90, 168, and 292 for the self-consistent calculations (filled circles and open triangles). For instance, the 1g and 2p shells are filled anew when the size increases from $N = 34$ to $N = 58$. We can find no correct self-consistent solution for closed-shell configurations in the size ranges where the connecting lines are missing. In the range $132 < N < 168$, for example, we can acquire no well defined solution for either $N = 138$ (with the 3p shell closed and the 1j shell empty) or $N = 162$ (with the 1j shell closed and the 3p shell empty). If we assume that the 3p shell is closed and the 1j shell is empty, the self-consistent calculation leads to the incorrect solution where the 3p level is higher than the 1j level, and vice versa. This difficulty may occur when one of two very close energy levels is occupied and the other is empty. No well defined solution can be determined for open-shell configurations in the neighbourhood of the insoluble closed-shell configuration either. We encounter the same difficulty in the LDA calculation of the conduction-electron ground state of small metal particles [3]. The

reason why we are confronted with this difficulty more often in the present calculation is that, as is mentioned below, the energy-level crossing often happens because the potential bending varies significantly with change of the size. This difficulty might be attributed to the LDA.
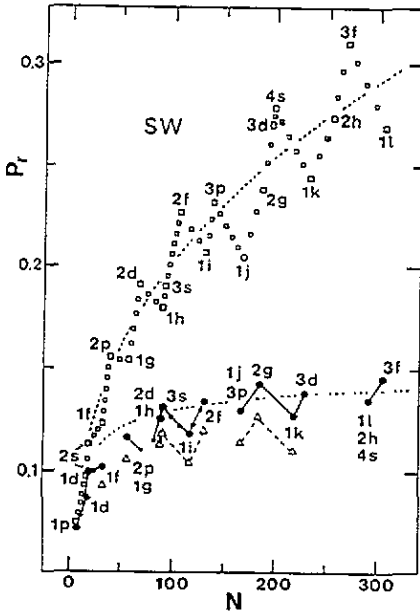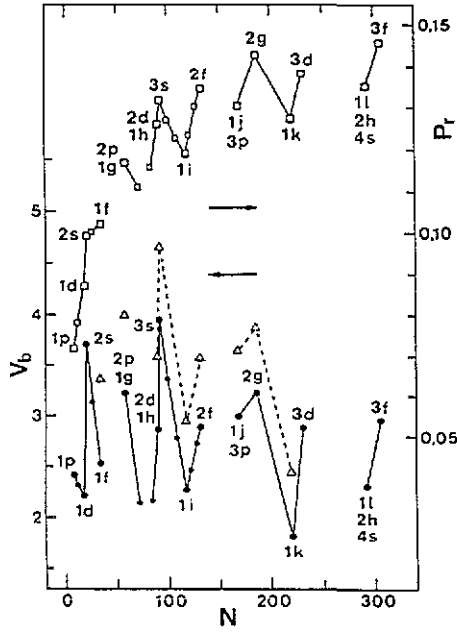

Figure 2. The size dependence of the radial dipole obtained from the full self-consistent calculation involving the image potential (filled circles), the self-consistent calculation taking no account of the image potential (open triangles), and the non-self-consistent calculation assuming the square-well potential (open squares).

Except for some filled circles in the smaller size range, the lower and upper broken curves in figure 2 smooth the oscillatory variation and give a rough description of the size dependence of P_r plotted by filled circles and open squares, respectively. The upper broken curve is obtained from the one-step carrier density distribution

$$n(r) = \begin{cases} [R/(R-t)]^3 n^+ & \text{for } r < R - t \\ 0 & \text{for } r > R - t \end{cases} \tag{16}$$

with $t/a_B^* = 0.43$. This density distribution is the simplest model to allow for the existence of the carrier-deficient surface layer and the surplus of carriers inside the surface layer. These two factors are essential to explain the averaged variation of the open squares. On the other hand, the lower broken curve is derived from the two-step density distribution

$$n(r) = \begin{cases} n^+ & \text{for } r < R - d \\ \dfrac{d(3R^2 - 3Rd + d^2)}{(d-t)[3R^2 - 3(t+d)R + (t^2 + td + d^2)]} n^+ & \text{for } R - d < r < R - t \\ 0 & \text{for } r > R - t \end{cases} \tag{17}$$

Figure 3. The size dependence of the magnitude of the downward potential bending in the presence of the image potential (filled circles) and in the absence of the image potential (open triangles), in comparison with the size dependence of the radial dipole involving the effect of the image potential (open squares).

with $t/a_B^* = 0.4$ and $d/a_B^* = 1.521$. The smoothed size dependence of the lower broken curve results from the existence of the carrier-deficient surface layer and the prominent peak in the profile and from charge neutrality inside the prominent peak.

The oscillatory variation of the radial dipole P_r reflects the sequential occupation from one shell to another with increasing size. The minimal turning point corresponds to the size where a shell of $n = 1$ and higher l becomes closed, while the maximal turning point corresponds to the size where a shell of $n \geqslant 2$ becomes closed. The upward or downward trend in the saw-tooth pattern of P_r depends upon where the shell getting filled has its substantial probability density. Here we pay attention to the result of the self-consistent calculations (see filled circles and open triangles). For example, as is stated above, the probability density of the 3s shell is quite well localized around the centre. In the upper panel of figure 1(h), the 2g shell constitutes the major part of the peak around $r/a_B^* \simeq 2.3$ in the g-component profile curve. The probability density of the 2g shell is concentrated well inside the particle. The radial dipole tends to increase when we are filling a shell that has its substantial probability density around the centre or well inside the particle. In contrast, the probability density of the 1i or 1k shell is well localized near the surface, as is shown by the i-component profile curve at $N = 118$ or the k-component profile curve at $N = 220$. The radial dipole tends to decrease when we are filling a shell whose probability density is concentrated near the surface.

In figure 2, we compare the size dependence of P_r in the presence of the image potential (filled circles) with that in the absence of the image potential (open triangles). As is mentioned above, if the image potential is switched off, a small fraction of internal carrier charges transfer to the surface region. This charge transfer is responsible for the downward

rigid shift of the saw-tooth pattern of P_r.

Here we turn our attention to the effective one-particle potential and the occupied energy levels (see the full curve and the full bars in each lower panel of figure 1(a)–(j)). The radial dependence of the effective potential is characterized by the downward bending and the steep ascent in the close vicinity of the surface. Figure 3 displays the size dependence of the potential bending V_b in the presence of the image potential (filled circles) and in the absence of the image potential (open triangles), in parallel with the size dependence of the radial dipole P_r involving the effect of the image potential (open squares). The plot of open squares is the same as that of filled circles in figure 2. The potential bending V_b is defined as the absolute value of the minimum of the effective potential V_{eff}. Note that the value of V_{eff} is measured from its value at $r = 0$. The values of V_b and P_r are scaled on the left and right ordinates, respectively. As in figure 2, larger filled circles, all open triangles, and larger open squares correspond to closed-shell configurations, while smaller filled circles and smaller open squares correspond to open-shell configurations. The newly occupied shell or shells are specified at each closed-shell point.

The potential bending varies remarkably with changing size. This variation involves a significant change of the relative energy-level position of the shells that have different probability density distributions. For example, when the size becomes larger from $N = 92$ to $N = 118$ with a great decrease of the potential bending, the energy-level crossing happens for two pairs of energy levels, namely, the 1f and 1g levels become higher than the 2s and 2p levels, respectively. When the size becomes still larger from $N = 118$ to $N = 132$ with an appreciable increase of the potential bending, the energy-level intersection occurs for the same two pairs of energy levels, that is, the 1f and 1g levels become lower than the 2s and 2p levels, respectively. The downward bending of V_{eff} forms a potential hollow near the surface. With increase (decrease) of the potential bending, the potential hollow becomes deeper (shallower), which lowers (heightens) the energy levels of the shells whose probability density is concentrated near the surface, particularly in the potential hollow.

Decomposition of the effective potential in figure 1(c) and (i) shows that the downward potential bending originates from the downward electrostatic Hartree potential V_H constructed from the charge density distribution due to negative carriers and positive donors (see equation (3)), and that the image potential V_{im} acts against the downward Hartree potential to suppress the downward potential bending and to make the effective potential quickly ascend in the close vicinity of the surface. The oscillatory profile of the carrier density reveals itself in the exchange–correlation potential as a small oscillatory variation.

Absence of the image potential enhances the downward potential bending and deepens the potential hollow, as is shown in figure 1(a), (d), and (g). This enhancement of the downward bending lowers especially the energy levels of the shells that have their substantial probability density near the surface. This energy shift is more pronounced at smaller sizes. As in figure 3, switching off the image potential produces an upward rigid shift of the saw-tooth pattern of the potential bending (compare the series of full circles with that of open triangles).

Figure 1(e) implies that, apart from some deviation, the Hartree scheme involving the image potential gives a good description of our carrier system, and that the exchange–correlation effect merely plays an auxiliary role, because our carrier system has a high effective density. Switching on the exchange–correlation potential gives rise to a slight enhancement of the peak near the surface and that around the centre in the carrier density profile, because the exchange–correlation potential becomes lower at higher carrier concentration.

Figure 3 shows that the size dependence of the potential bending bears a *striking*

resemblance to that of the radial dipole. The saw-tooth pattern of the potential bending also reflects the serial occupation from one shell to another with increasing size. We examine how each shell contributes to the downward potential bending through its characteristic probability density distribution. The downward bending of the effective potential originates from the downward electrostatic Hartree potential. Figure 4 exhibits the Hartree potential V_{H} (full curve) and its decomposition into constituent shell components (dotted curves) for $N = 58$. Each dotted (n, l) curve represents the electrostatic potential which is generated by the charge density distribution $n(r; nl) - n^+(nl)$, where $n(r; nl)$ and $n^+(nl)$ denote, respectively, the (n, l) component of the carrier density and the constant component of the uniform donor density which cancels with $n(r; nl)$ as a whole. This charge neutrality as a whole requires the derivative of each dotted curve to vanish at the surface. Each potential curve is measured from its value at the centre. In comparing figure 4 with the upper panel of figure 1(b), we can understand how the character of the probability density distribution of each (n, l) component is correlated with that in its corresponding potential curve. As is seen from inspection of the 2s or 2p shell, the downward potential is created by the probability density which is localized around the centre or well inside the particle. This downward potential acts to enhance the downward bending of V_{eff}. As is obvious from inspection of the 1f or 1g shell, the upward trend is dominant in the potential curve produced by the probability density that is concentrated near the surface. This upward trend operates to suppress the downward bending of V_{eff}. Thus it is established that the value of V_{b} increases when we are filling a shell whose substantial probability density is localized around the centre or well inside the particle, and that the value of V_{b} decreases when we are occupying a shell whose substantial probability density is concentrated near the surface.
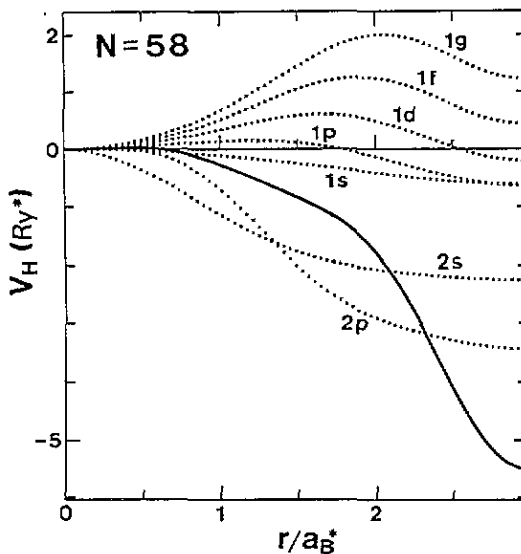

Figure 4. Decomposition of the electrostatic Hartree potential V_{H} (full curve) into the constituent shell components (dotted curves) for $N = 58$.

In the case of the semi-infinite geometry, the downward potential bending at the flat neutral surface for the same carrier concentration is estimated to be ~ 3.8 in units of $\mathrm{Ry}^* = e^2/2\varepsilon_0 a_{\mathrm{B}}^*$ by means of a parametric Hartree calculation taking no account of the

image potential (see figure 5 in [17]). As evaluated from figures 3 and 1(e), the effects of the image potential and the exchange–correlation potential would reduce the above value of the downward bending to a smaller reasonable value which is compatible with the variation of the filled circles in figure 3.

So far we have been concerned with electrically neutral particles. Here we examine how the carrier ground state varies when the number of carriers is not balanced with that of ionized donors. This examination may be helpful to understand the case where our particle system can exchange carriers with its surroundings or its surface states. In the same manner as in figure 1, figure 5 displays the carrier ground state for $N = 118$ and $N_D = 98$ (a) and that for $N = 118$ and $N_D = 133$ (b), where N and N_D denote the number of carriers and that of donors, respectively. The dotted curve and line in each upper panel of figure 5 represent, respectively, the carrier density profile and the homogeneous donor density for the neutral particle. The dotted curve and bars in each lower panel of figure 5 indicate, respectively, the effective potential and the occupied energy levels for the neutral particle. Each of the occupied energy levels for the neutral particle is assigned just outside the right ordinate. The result for the neutral particle is the same as in figure 1(e). These donor-deficient and donor-superfluous particles have the same carrier configuration as the neutral particle. When the donor density level shifts down with decrease of N_D (see figure 5(a)), internal excess carriers transfer to the surface region to try to achieve charge neutrality inside the prominent peak in the carrier density profile and to screen the positive charges in the carrier-deficient surface layer. Deepening of the potential hollow near the surface makes the 1f and 1g levels lower than the 2s and 2p levels, respectively. On the other hand, when the donor density level shifts up with increase of N_D (see figure 5(b)), there occurs an opposite carrier transfer from the surface region to the interior, to tend towards charge neutrality inside the prominent peak. Owing to shallowing of the potential hollow, the 1h level becomes higher than the 2d level.

4. Summary

We have investigated the size dependence of the carrier ground state of small spherical semiconductor particles with the doping level fixed. The particles are assumed to be in an insulating medium or in the vacuum and to be electrically neutral as a whole. The results are summarized as follows.

(1) The carrier density distribution. The most pronounced feature in the carrier density profile regardless of the size is the existence of the prominent peak near the surface and the carrier-deficient surface layer immediately outside the peak. The Friedel oscillation inside the prominent peak is quite outstanding in the smaller size range, and its variation with increasing size can be understood by taking account of the probability density distribution of the newly occupied shell and the volume extension of carrier states in the already closed shells. With increasing size, this Friedel oscillation becomes less and less conspicuous, which reduces to the nearly constant density balanced with the uniform donor density. Free carriers tend to attain charge neutrality inside the prominent peak, and superfluous carriers, if any, tend to transfer to the surface region to screen the positive charges in the carrier-deficient surface layer.

(2) The effective one-particle potential. The magnitude of the downward potential bending makes a striking oscillatory variation with increasing size. This variation reflects the sequential occupation from one shell to another. The upward or downward trend in this variation depends upon whether the newly filled shell has its substantial probability density
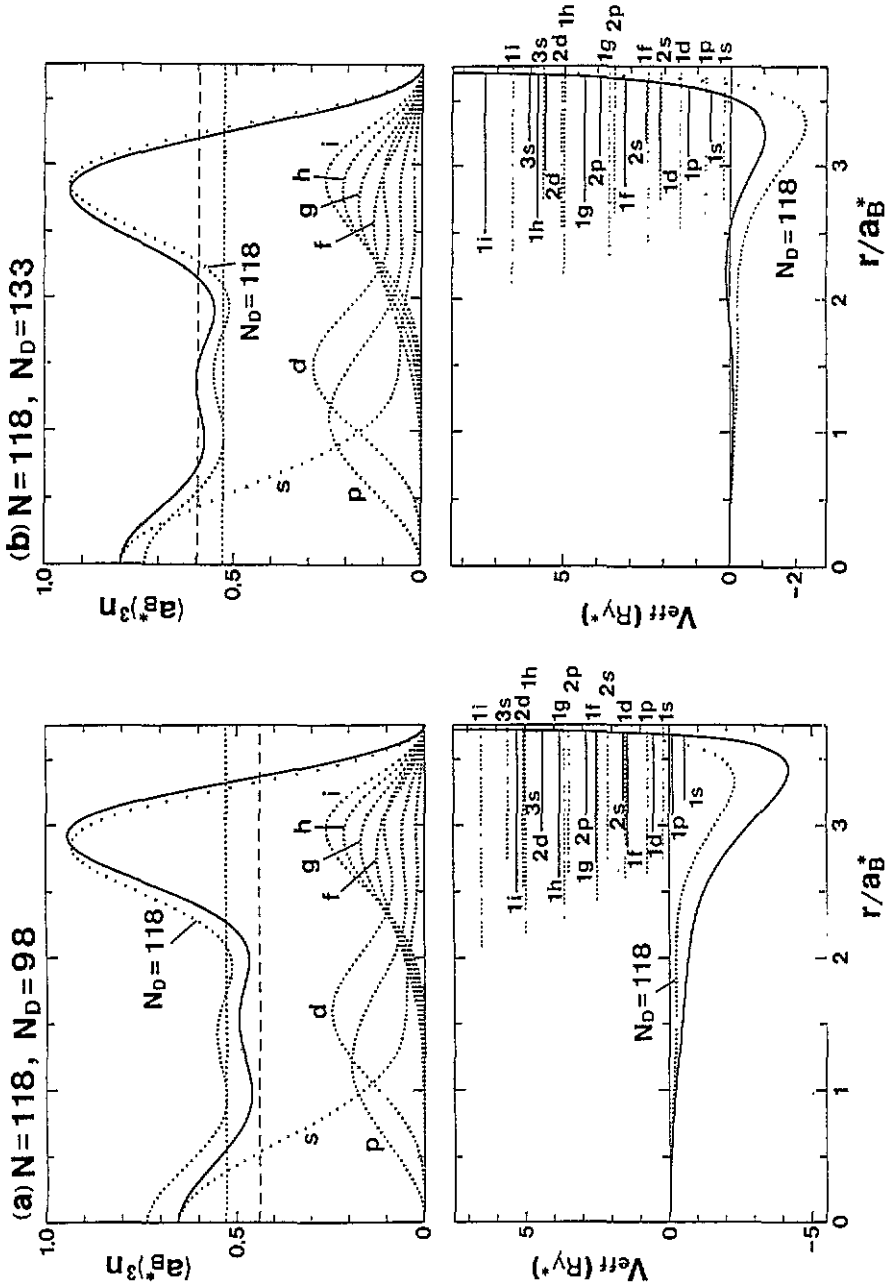
Figure 5. The carrier ground state for $N = 118$ in the donor-deficit case $N_D = 98$ (*a*) and in the donor-surplus case $N_D = 133$ (*b*), compared with the neutral case $N_D = 118$. For details, see the text.

around the centre (well inside the particle) or near the surface. Owing to the significant variation of the potential bending, the energy intersection often happens between two close energy levels with different angular momenta *l*.

By varying the number of donors, we have also explored the carrier ground state of donor-deficient and donor-superfluous particles which have the same carrier configuration as the neutral particle. With changing donor number, a carrier transfer occurs between the interior and the surface region to tend towards charge neutrality inside the prominent peak in the carrier density profile. Decrease of the donor number enhances the downward potential bending significantly, which often entails the energy intersection of two close energy levels with different angular momenta *l*.

The present analysis has assumed perfectly spherical particles, which leads to the high degeneracy of angular-momentum states. Here we comment upon what happens when the particle shape deviates from the perfect sphere. To understand the size dependence of the carrier ground state in the present analysis, it is essential to note that each shell has its own characteristic probability density distribution. Departure from the complete sphere will give rise to shell splitting into subshells or separate levels. This shell splitting may operate to smear the shell effects in the size dependence that are quite clear in the case of a perfect sphere. However, the essential part of our results will survive, apart from some quantitative modification, if these subshells or levels retain the same character in the probability density distribution as their original shell.

Acknowledgments

References

[1]   Ekardt W 1984 *Phys. Rev.* B **29** 1558
[2]   Beck D E 1984 *Solid State Commun.* **49** 381
[3]   Puska M J, Nieminen R M and Manninen M 1985 *Phys. Rev.* B **31** 3486
[4]   Ishii Y, Ohnishi S and Sugano S 1986 *Phys. Rev.* B **33** 5271
[5]   Beck D E 1984 *Phys. Rev.* B **30** 6935
[6]   Kresin V 1989 *Phys. Rev.* B **39** 3042
[7]   Ekardt W 1985 *Phys. Rev.* B **32** 1961
[8]   Serra Ll, Garcias F, Barranco M, Navarro J, Balbás C and Mañanes A 1989 *Phys. Rev.* B **39** 8247
[9]   Saito S, Bertsch G F and Tománek D 1991 *Phys. Rev.* B **43** 6804
[10] Knight W D, Clemenger K, de Heer W A, Saunders W A, Chou M Y and Cohen M L 1984 *Phys. Rev. Lett.* **52** 2141
[11] Knight W D 1990 *The Chemical Physics of Atomic and Molecular Clusters* ed G Scoles (Amsterdam: North-Holland) p 413
[12] Srivastava K S, Tandon A, Trivedi M and Fatima N 1989 *Physica* B **159** 295
[13] Sasaki Y, Nishina Y, Sato M and Okamura K 1989 *Phys. Rev.* B **40** 1762
[14] Yamamoto K, Kimura K, Ueda M, Kasahara H and Okada T 1985 *J. Phys. C: Solid State Phys.* **18** 2361
[15] Inaoka T 1992 *J. Phys.: Condens. Matter* **4** L601
[16] Kohn W and Sham L J 1965 *Phys. Rev.* **140** A1133
[17] Baraff G A and Appelbaum J A 1972 *Phys. Rev.* B **5** 475

[18]   Ando T 1975 *J. Phys. Soc. Japan* **39** 411
[19]   Gunnarsson O and Lundqvist B I 1976 *Phys. Rev.* B **13** 4274
[20]   Inaoka T 1993 *unpublished*